EUROFUSION WPMST1-PR(16) 16488

D Reiser et al.

Drift-based scrape-off particle width in X-point geometry

Preprint of Paper to be submitted for publication in Nuclear Fusion

This work has been carried out within the framework of the EUROfusion Consortium and has received funding from the Euratom research and training programme 2014-2018 under grant agreement No 633053. The views and opinions expressed herein do not necessarily reflect those of the European Commission.

Drift-based scrape-off particle width in X-point geometry

D. Reiser[1] and T. Eich[2]
[1]Forschungszentrum Jlich GmbH, Institut fr Energie- und Klimaforschung Plasmaphysik, Partner of the Trilateral Euregio Cluster (TEC), 52425 Jlich, Germany
[2]Max-Planck-Institut für Plasmaphysik, Boltzmannstr. 2, 85748 Garching, Germany

The Goldston heuristic estimate of the scrape-off layer width (Nucl. Fusion 52, 013009, 2012) is reconsidered using a fluid description for the plasma dynamics. The basic ingredient is the inclusion of a compressible diamagnetic drift for the particle cross field transport. Instead of testing the heuristic model in a sophisticated numerical simulation including several physical mechanisms working together, the purpose of this work is to point out basic consequences for a drift-dominated cross field transport using a reduced fluid model. To evaluate the model equations and prepare them for subsequent numerical solution a specific analytical model for 2D magnetic field configurations with X-points is employed. In a first step parameter scans in high-resolution grids for isothermal plasmas are done to assess the basic formulas of the heuristic model with respect to the functional dependence of the scrap-off width on the poloidal magnetic field and plasma temperature. Particular features in the 2D-fluid calculations - especially the appearance of supersonic flows - are discussed and can be understood in the framework of a reduced 1D model. The resulting semi-analytical findings might give hints for experimental proof and implementation in more elaborated fluid simulations.

I. INTRODUCTION

The heuristic model of Goldston [1] has attracted much interest and discussion in the studies of scrape-off layer power width and has been compared with several experimental results [2; 3]. However, its analytical framework does not take into account several details of the magnetic field shaping, parallel flow balances, electric fields and neutral physics. The purpose of this contribution is to complement the heuristic estimate of Goldston and to assess the particular implications of the drift-based radial particle transport for the scrape-off layer (SOL) width in an axisymmetric tokamak geometry including an X-point. The basic ideas of Goldston's approach are rewritten as a reduced 2D fluid model taking into account particle balance and parallel momentum balance in an isothermal plasma. The basic ingredient is the inclusion of a compressible diamagnetic drift for the particle cross field transport. Numerical solution of this reduced transport model shows that

(1) the specifics of the drift-based radial transport introduces particle and momentum sinks in the SOL dynamics causing supersonic flows - contrary to diffusive seeding of the SOL.

(2) in standard ASDEX Upgrade geometry the SOL width is often well approximated by a constant decay length Λ, characterizing an exponential decay of particle density with respect to the flux label coordinate.

(3) the basic dependencies of SOL width on the poloidal Larmor radius remain unchanged in X-point geometries.

The second result justifies the reduction to a 1D model and it is shown that the resulting semi-analytical predictions reproduce quite well the findings of the 2D simulations, in particular the supersonic transitions. Moreover, it offers an alternative derivation for Goldston's estimate and can be extended easily to an estimate including additional particle diffusion, therefore giving boundaries for detailed studies of the drift-based transport with more sophisticated fluid simulations.

The paper is structured as follows: In Section II the basic equations of the 2D fluid model are presented and in Section III the model tokamak geometry for the numerical simulations are elucidated. Results for the density profiles and flow velocities obtained by numerical solution of the 2D model are presented and discussed in Section IV. Justified by these 2D results a 1D model reduction is derived and presented in Section V. In Section VI further results from 2D simulations for varying plasma parameters are presented, discussed and compared with the predictions of the reduced 1D model. In Section VII also the effect of an additional diffusive particle transport is discussed on the basis of 2D simulations and a simple extension of the 1D model as well. The concluding Section VIII summarizes the results of this paper.

II. FLUID FORMULATION OF GOLDSTON'S HEURISTIC MODEL

To study the consequences of Goldston's ideas on the drift-based SOL width in a tokamak geometry with X-point and asymmetrical shaping a simplified model is considered translating the ideas of the heuristic model presented in [1] to a 2D fluid picture for the plasma dynamics. In a first stage the model consists of the balance equations for particles and parallel ion momentum. The electron and ion temperatures are assumed to be equal and prescribed. Currents are neglected, i.e. $\mathbf{u} = \mathbf{v}$, where $\mathbf{u}$ is the ion flow velocity and $\mathbf{v}$ the electron velocity. The model equations for the particle density n and the parallel ion velocity $u_\parallel$ read

$$\frac{\partial n}{\partial t} + \boldsymbol{\nabla} \cdot (n\mathbf{u}_\parallel) + \boldsymbol{\nabla} \cdot (n\mathbf{u}_*) = S_n \tag{1}$$

$$\frac{\partial}{\partial t}\left(nu_{\parallel}\right)+\boldsymbol{\nabla}\cdot\left(n\mathbf{u}_{\parallel}u_{\parallel}\right)=-\frac{2\nabla_{\parallel}p}{m_i} \tag{2}$$

where

$$\mathbf{u}_{*}=\frac{\mathbf{B}\times\boldsymbol{\nabla}p}{enB^2} \tag{3}$$

denotes the ion diamagnetic drift and $u_{\parallel}$ is the parallel ion velocity. The divergence of the diamagnetic particle flux can be rewritten due to the following relation

$$\boldsymbol{\nabla}\cdot(n\mathbf{u}_{*})=\boldsymbol{\nabla}\cdot\left(\frac{\mathbf{B}\times\boldsymbol{\nabla}p}{eB^2}\right)=\boldsymbol{\nabla}\cdot(n\mathbf{u}_{\times})=\mathbf{u}_{\times}\cdot\frac{\boldsymbol{\nabla}p}{T} \tag{4}$$

The velocity $\mathbf{u}_{\times}$ is given as

$$\mathbf{u}_{\times}=\frac{T}{e}\boldsymbol{\nabla}\times\frac{\mathbf{B}}{B^2}=\frac{2T}{eB}\frac{\mathbf{B}\times\boldsymbol{\nabla}B}{B^2}+\frac{T}{e}\frac{\boldsymbol{\nabla}\times\mathbf{B}}{B^2} \tag{5}$$

and is representing the particle guiding center drifts in an inhomogeneous magnetic field [4; 5].

III. MODEL MAGNETIC FIELD CONFIGURATION

An axisymmetric magnetic field $\mathbf{B}$ is described in right-handed orthogonal coordinates (r,θ,ϕ) by

$$\mathbf{B}=B^{\theta}\,\mathbf{e}_{\theta}+B^{\phi}\,\mathbf{e}_{\phi} \tag{6}$$

The coordinate r is a flux label. For a divergence free field, i. e.

$$\boldsymbol{\nabla}\cdot\mathbf{B}=\frac{1}{J}\frac{\partial}{\partial\theta}\left(JB^{\theta}\right)=0 \tag{7}$$

the poloidal component B^{θ} must be of the form

$$B^{\theta}=\frac{B_0\,C}{J} \tag{8}$$

where $C=C(r)$ is a flux label too, B_0 is a constant and J=$\mathbf{e}_r\cdot\mathbf{e}_{\theta}\times\mathbf{e}_{\phi}$ is the Jacobian. The function $C(r)$ is directly related to the plasma current I_p and can be chosen by requiring a particular value for the flux surface averaged physical poloidal field $\langle\hat{B}_{\theta}\rangle$ at the separatrix according to an experimental setup and using the approximate formula

$$\langle\hat{B}_{\theta}\rangle=\frac{\mu_0 I_p}{2\pi a\sqrt{(1+\kappa^2)/2}} \tag{9}$$

where a is the minor radius and κ denotes the elongation [**?**]. The toroidal component is chosen in a tokamak like form

$$B^{\phi}=\frac{B_0R_0}{R^2} \tag{10}$$

where the functional relation for R as a function of r and θ is given in the Appendix A by Eq. A2. The detailed definition of the coordinates (r,θ,ϕ) based on a conformal map is also presented in Appendix A. The explicit form of the model equations Eqs. 1-2 for these coordinates is

$$\frac{\partial n}{\partial t}+\frac{1}{J}\frac{\partial}{\partial\theta}\left(J\frac{B^{\theta}}{B}nu_{\parallel}+Jnu_{\times}^{\theta}\right)+\frac{1}{J}\frac{\partial}{\partial r}\left(Jnu_{\times}^{r}\right)=S_n \tag{11}$$

$$\frac{\partial}{\partial t}\left(m_i nu_{\parallel}\right)+\frac{1}{J}\frac{\partial}{\partial\theta}\left(J\frac{B^{\theta}}{B}m_i nu_{\parallel}^2\right)=-\frac{2B^{\theta}}{B}\frac{\partial p}{\partial\theta} \tag{12}$$

where the contravariant components of $\mathbf{u}_{\times}$ are

$$u_{\times}^{r}=-\frac{2T}{eB}\frac{B_{\phi}}{JB^2}\frac{\partial B}{\partial\theta},\quad u_{\times}^{\theta}=\frac{2T}{eB}\frac{B_{\phi}}{JB^2}\frac{\partial B}{\partial r}, \tag{13}$$

The magnetic field geometry considered in this work is sketched in Fig. 1 left, and profiles of the physical radial component $\mathbf{u}_{\times}$ for this configuration are shown in Fig. 2 and in Fig. 3 top.

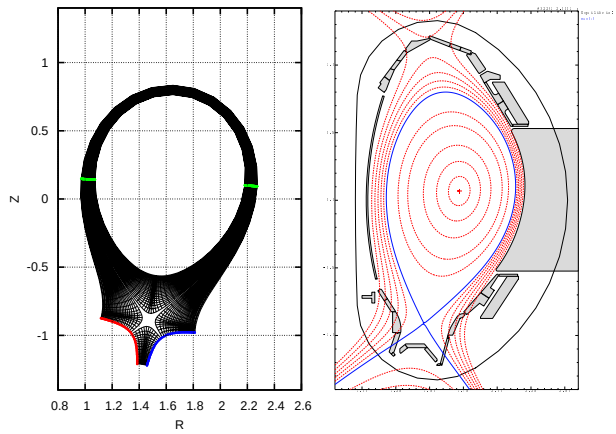

FIG. 1 Model geometry for ASDEX like magnetic field based on the conformal mapping presented in the Appendix A. On the left the computational domain (with reduced number of grid points to for clarity) is shown for R_0=1.65 m, h=1.2 m and rotation angle ξ=-0.15. The points in red label the inner target (θ=-0.7), the points in blue the outer target (θ=6.98). The separatrix is located at r=h and $0\leq\theta\leq2\pi$. The X-point is located at θ=0 and θ=2π, respectively. The right figure shows the equilibrium reconstruction of ASDEX Upgrade shot No. 32291 at t=2 s serving as a template for the conformal map in the left figure.

IV. 2D SIMULATIONS IN X-POINT GEOMETRY

The model equations Eqs. 11 and 12 are solved numerically on orthogonal (r,θ)-grids of size $N_r\times N_{\theta}$=200×100 prepared by the conformal map of Appendix A. A sketch of the computational grid (less resolution than used in the simulations) is shown in Fig. 1. Standard second order discretization is used for the spatial derivatives. For the time stepping a second order Runge-Kutta-scheme and a time step Δt=1.0·10^{-8} is employed. The

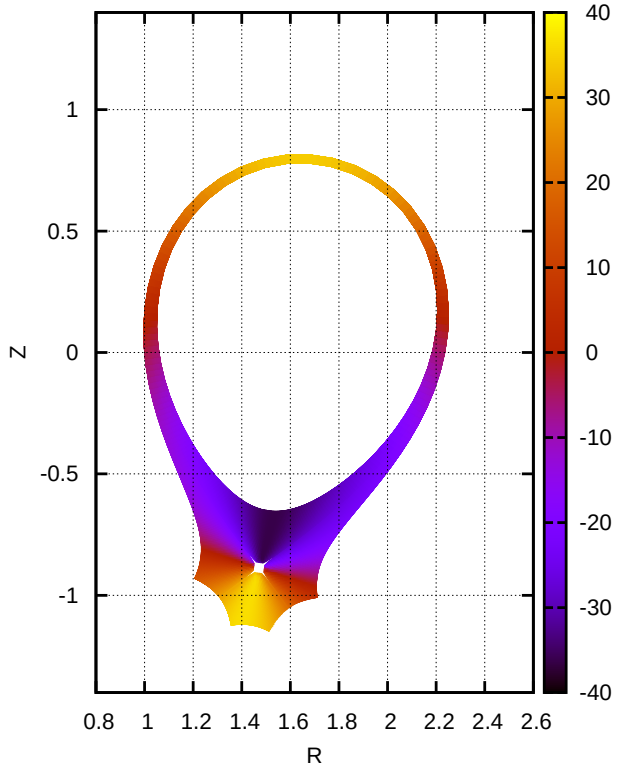

FIG. 2 Physical component of the radial component of velocity $\mathbf{u}_\times$ defined by Eq. 5 being responsible for advection of particles into and out of the SOL for the model geometry used in this work and sketched in Fig. 1.

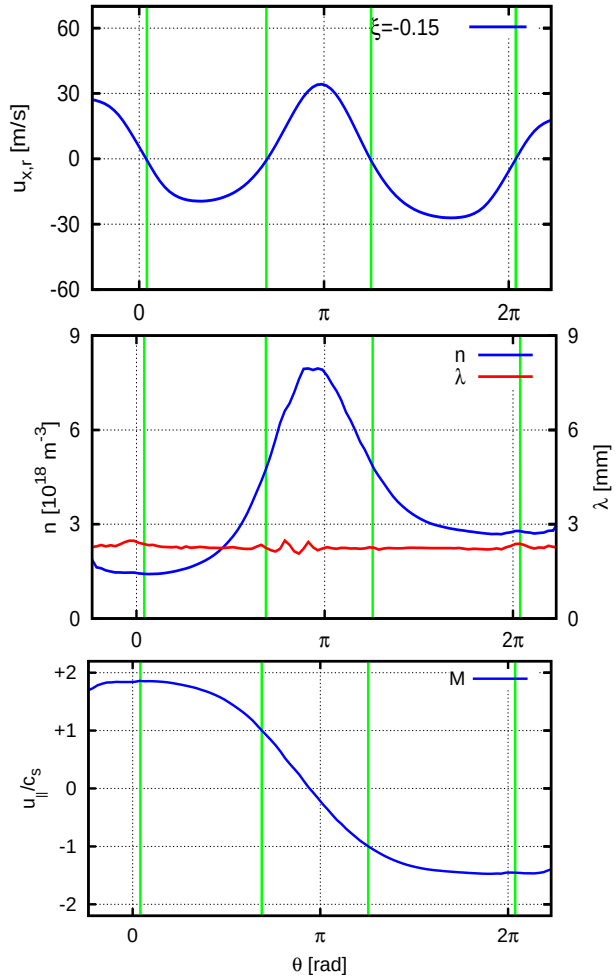

FIG. 3 (Color online) From top to bottom: profiles of the radial physical component of the drift velocity $\mathbf{u}_\times$, the density n and Mach number vs poloidal angle θ for the magnetic field configuration with ξ=-0.15. The green lines label the points where $u_\times^r$=0. Additionally the center plot includes the profile of the decay length Λ given by the numerical values of $|\partial \ln n/\partial r|^{-1}$.

Kurganov-Tadmor central semi-discrete scheme is used for the conservative part of the evolution equations [6]. At the targets sheath boundary conditions are imposed, i. e. $\partial n/\partial\theta$=0 and $u_\parallel$=$\pm c_s$, where c_s^2=$\sqrt{2T/m_i}$ defines the sound speed. For the outer boundary zero derivatives are assumed for n and $u_\parallel$ and at the separatrix the density is prescribed by a constant value $2{\cdot}10^{19}$ m^{-3}, whereas the velocity gradient is set to zero, $\partial u_\parallel/\partial r$=0. The time evolution of density n and flow velocity $u_\parallel$ is followed until a stationary state is obtained. The parameters chosen were R_0=1.65 m, h=1.2 m, C=0.2785, B_0=2.5 T, T=75 eV and an ion mass m_i=2 m_p. The value for C provides a separatrix averaged value $\langle\hat{B}_\theta\rangle$=-0.28 T. The rotation angle ξ has been chosen as -0.15 and additionally for some cases a change in the direction of the toroidal field has been considered. The Fig. 3 shows results for the stationary profiles $n(\theta)$ and $u_\parallel(\theta)$ at r=1.0042 h, i. e. inside the SOL and close to the separatrix. The corresponding radial profiles of the density $n(r)$ at the inner and outer target and the inner and outer midplane are shown in Fig. 4. The density profile in Fig. 3 shows a pronounced maximum occuring in the central region where the radial velocity $u_\times^r$ is positive, therefore providing an inflow from the core plasma into the SOL (see Fig. 3 top). One might expect that the poloidal component of $\mathbf{u}_\times$ might introduce a flow reversal due to the appearance of Pfirsch-Schlüter flows. Actually the poloidal component of $\mathbf{u}_\times$ is more than 2 orders of magnitude smaller than the poloidal projection of sound speed and does not have a significant impact on the parallel flow. The most striking result is the appearance of supersonic flows with Mach number M=$u_\parallel/c_s$, c_s^2=$2T/m_i$, being above 1 or less than -1 in the velocity profile (Fig. 3 bottom). A very important result of the 2D simulations is an almost exponential decay of the density $n{\sim}e^{-r/\Lambda}$ with respect to the flux label r and Λ being almost constant along θ inside the SOL and not to close to the separatrix. This is illustrated by the red colored line in the mid figure of Fig. 3 showing Λ=$|\partial \ln n/\partial r|^{-1}$ and by the logarithmic plots in Fig. 4 bottom. Right at the separatrix the results are considered as less significant, because the fixed particle density boundary condition there is probably not well suited to get a realistic picture for the inflow/outflow conditions. For this reason the following discussion is

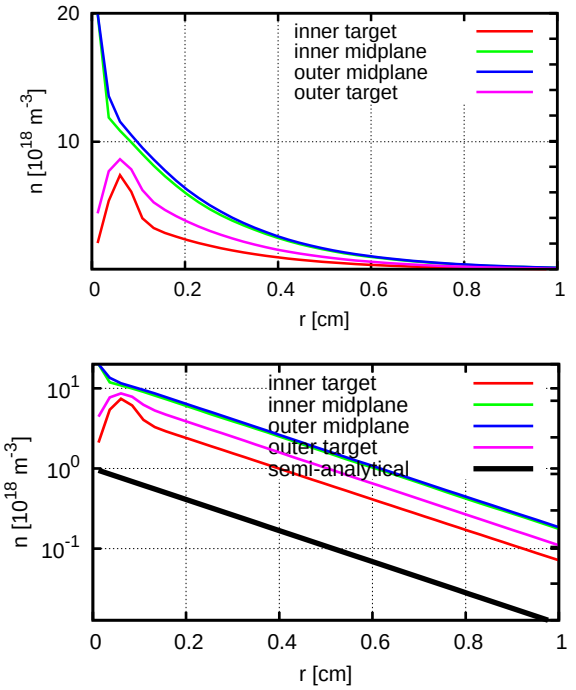

FIG. 4 (Color online) Profiles of density n at the inner and outer target and the inner and outer midplane in linear (top) and logarithmic (bottom) representation. The black line in the bottom figure is the fitting curve $e^{-r/\Lambda}$ where the averaged value of Λ shown in Fig. 3 is used.

restricted to the region r>1.0042 h, where boundary effects do not play a significant role anymore (this has been proved by the use of different boundary conditions).

V. 1D MODEL REDUCTION

Justified by the results of the 2D simulation described in the section above it is assumed that

$$\frac{\partial n}{\partial r} = -\frac{n}{\Lambda} \tag{14}$$

where Λ=const. Note that the physical decay length λ is given by $\lambda=\sqrt{g_{rr}}\Lambda$, where the square root of the metric coefficient g_{rr} determines the flux expansion factor f_x often used in the analysis of scrape-off widths [2]. The flux expansion f_x can be understood as the ratio between the values of $\sqrt{g_{rr}}$ at the target and the outer midplane. Furthermore, the model equations Eqs. 11-12 are simplified by neglecting the poloidal component of the velocity $\mathbf{u}_\times$, any particle sources S_n and the terms due to the parallel variation of B (except in the diamagnetic effects). These assumptions were justified a posteriori by switching off the particular terms in the 2D simulations and proving that the results were not significantly changed. Based on these assumptions the stationary case is described by a one-dimensional model

$$u_\parallel \frac{\partial n}{\partial \theta} = -n\frac{\partial u_\parallel}{\partial \theta} + \frac{B}{B^\theta}\frac{u_\times^r}{\Lambda} n \tag{15}$$

$$u_\parallel \frac{\partial u_\parallel}{\partial \theta} = -\frac{2T}{m_i}\frac{\partial n/\partial \theta}{n} \tag{16}$$

Combining these equations, and using the Mach number $M=u_\parallel/c_s$ and the logarithmic density $N=\ln n$ as dependent variables, one obtains

$$(1-M^2)\frac{\partial M}{\partial \theta} = F, \quad F = \frac{B}{B^\theta}\frac{u_\times^r}{\Lambda c_s} \tag{17}$$

$$\frac{\partial N}{\partial \theta} = -M\frac{\partial M}{\partial \theta} \tag{18}$$

The solutions of Eqs. 17 and 18 are

$$M - \frac{M^3}{3} = K, \quad K = \int \frac{B}{B^\theta}\frac{u_\times^r}{\Lambda c_s}\, d\theta + C_M \tag{19}$$

$$N = -\frac{M^2}{2} + C_N \tag{20}$$

where C_M and C_N are constant. Depending on the particular value of K different solution branches for Eq. 19 and thus bifurcations are possible as illustrated by Fig. 5. Inspection of Eq. 17 shows that the points where the drift velocity u_x^r is zero are of special interest because there $\partial M/\partial\theta$=0 and/or M=±1. Thus, if F=0 and $\partial M/\partial\theta$ and $\partial F/\partial\theta$ are finite, a transition occurs to supersonic parallel flow with $|M|$>1. Differentiation of Eq. 17 gives a relation valid for such transition points

$$\left.\frac{\partial F}{\partial \theta}\right|_{|M|=1} = -2M\left(\frac{\partial M}{\partial \theta}\right)^2 \tag{21}$$

and it follows that if F=0 at a particular point and $\partial F/\partial\theta$>0 only a supersonic transition through M=-1 is possible, whereas $\partial F/\partial\theta$<0 is compatible only with a transition through M=+1. A situation relevant for the

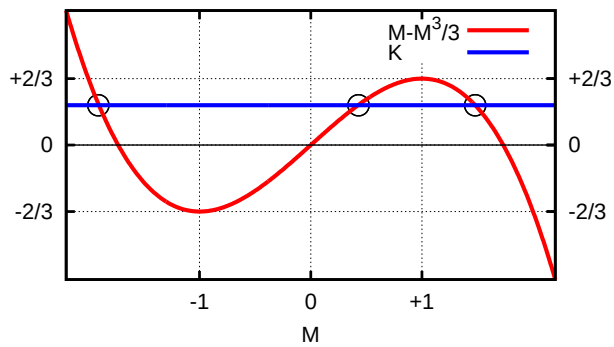

FIG. 5 (Color online) Illustration of a graphical solution of Eq. 19. If $|K|$<2/3 three solutions exist (example K=0.4 labeled by circles). For $|K|$=2/3 two solutions exist and for $|K|$>2/3 only a single real solution is possible.

drift-based transport considered in this work is the existence of - at least - two possible transition points where $u_\times^r$=0 (see Fig. 3 top). This is due to the fact that the

diamagnetic flows always introduce both, regions of particle inflow and outflow in the SOL. Requiring $M=\pm 1$ at two consecutive transition points, with $u_\times^r$ not changing sign between these points, a conditional equation for the decay length Λ results from Eq. 17

$$\Lambda = \frac{3}{4}\int \left| \frac{B}{B^\theta}\,\frac{u_\times^r}{c_s} \right| d\theta \tag{22}$$

The integral is taken from one transition point to the next one. This situation with two consecutive transition points corresponds to the result for the Mach number M shown in Fig. 3 bottom, where the green lines label the special points where $u_\times^r=0$. Using Eq. 22 the solution branches of Eq. 19 can be calculated. The possible solutions for $|M|=1$ appearing at two points along the magnetic field line are sketched in Fig. 6 by dotted lines and compared with the results from the 2D simulations of Fig. 3. The solution of the 2D simulations follow closely the smooth solution branch of Eq. 19 connecting the points of supersonic transition. Also the density profile agrees well with the result $n \sim e^{-M^2/2}$. The agreement is optimal for the region between the two transition points, where the particles are pushed across the sparatrix into the SOL (highlighted in green in Fig. 6). Outside this region the agreement is not as good, but still the 1D result gives a good qualitative description of the solution found in the detailed 2D simulation. Therefore, the analysis of the 1D reduced model explains the supersonic flows in the results presented above. Of course, not all features can be covered by the 1D consideration, in particular because the assumption of a constant Λ is not always justified for different magnetic field configurations. However, the basic features of the profiles found by 2D simulations are very well understood in the light of the analysis of the simplified 1D model and, therefore, it provides a good approximation for semi-analytical considerations. Finally, it should be noted that for cylindrical geometry the integral in Eq. 22 can be estimated via

$$u_\times^r \approx \frac{2T}{eBR_0}\sin\theta, \quad B^\theta \approx \frac{\hat{B}_\theta}{a} \tag{23}$$

where a is the minor radius and $\hat{B}_\theta$ the physical component of the poloidal magnetic field. Integration for $0 \le \theta \le \pi$ gives for the scrape-off width

$$\Lambda = \frac{3aT}{e\hat{B}_\theta R_0 c_s} \tag{24}$$

and this result is - despite a factor of 4/3 - identical with Goldston's estimate for λ for singly charged ions and atomic mass of 2 (Eq. 1 in [1]). Thus, the assumption of supersonic transitions in the fluid model considered here offers an alternative derivation of Goldston's estimate for the scrape-off width. However, at this point it is important to note that the simple expression Eq. 22 - and even more the estimate Eq. 24 - giving a quick estimate for the SOL width and building a bridge to Goldston's approach has to be used with care. To illustrate the subtleties just one additional example of 2D simulations and the related 1D approximation should be discussed here: the case with the same parameters used to obtain the results of Figs. 3, 4 and 6, but with direction of the toroidal field reversed. The results analogous to Fig. 3 are shown in Fig. 7. The basic change in the setup occurs in the sign of the velocity $\mathbf{u}_\times$, such that the top figure shows just the same velocity profile as top figure in Fig. 3 but with reversed sign. However, the results for the density and Mach number profiles shown in the center bottom figure are very different to the case discussed above. Now two maxima appear in the density profile, corresponding to the particle feeding in the two regions with $u_\times^r>0$ and the velocity profile shows a jump in the center region close to $\theta=\pi$. Now supersonic transitions occur at different locations and also a minimum, i. e. $\partial M/\partial\theta=0$, appears at a point with $u_\times^r=0$. The most important differences with respect to the estimates discussed above is the smaller value for Λ found in the 2D simulations (the red curve in the center plot). A closer inspection of these results shows that this reduced SOL width (Λ=1.23 mm instead of Λ=2.24 mm in the case discussed above) can be related again to Eq. 22 but now for the points at θ=3.94 and θ=6.40 connecting two supersonic transitions. It might be speculated that the inflow regions with $u_\times^r>0$ determine the velocity profile and therefore transition points and SOL width

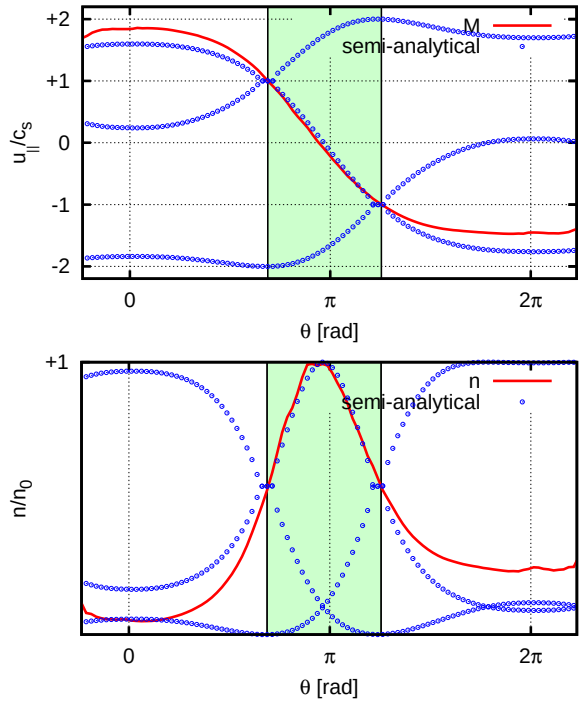

FIG. 6 (Color online) Profiles of Mach number and density vs poloidal angle θ already shown in Fig. 3 but here complemented by the results of Eq. 19. The region between the two transition points is highlighted in green.

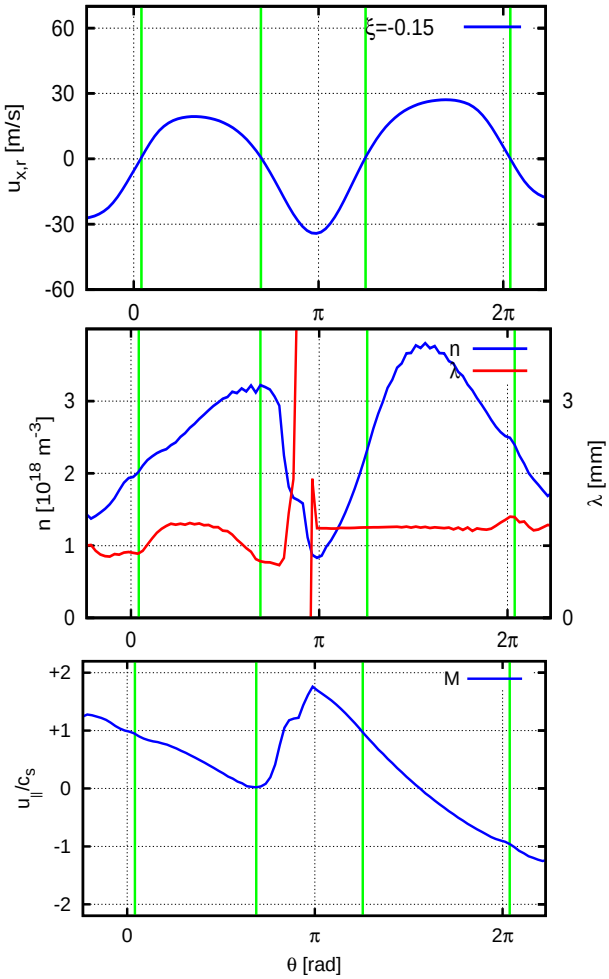

FIG. 7 (Color online) Simulation for the parameters chosen for Fig. 3 but with reversed toroidal magnetic field. From top to bottom: profiles of the radial physical component of the drift velocity $\mathbf{u}_\times$, the density n and Mach number vs poloidal angle θ for the magnetic field configuration with ξ=-0.15. The green lines label the points where $u_\times^r$=0. Additionally the center plot includes the profile of the decay length Λ given by the numerical values of $|\partial \ln n/\partial r|^{-1}$.

Λ. But the reason why the dynamical system is choosing this region and not the other inflow region and why $\partial M/\partial\theta$=0 is resulting at one point and not $|M|$=1 is not clear up to now. But this example demonstrates that the details of the X-point geometry have a significant impact on the SOL width, which is not taken into account in a formula like Eq. 24. On the contrary it must be stressed that the 1D reduced model derived here has been confirmed a posteriori using the numerical 2D findings but for an extended discussion also the principal mechanism for the Mach number profile to fulfill the general condition Eq. 17 must be known to get a more quantitative picture.

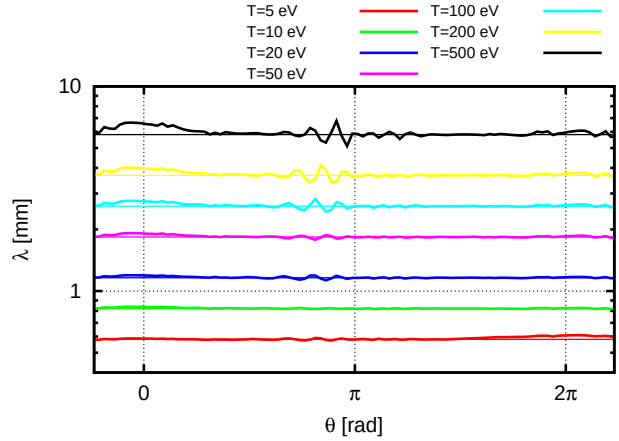

FIG. 8 (Color online) Dependence of Λ on the electron temperature T_e. Shown are the profiles of the inverse logarithmic derivatives $|\partial \ln n/\partial r|^{-1}$ overlaid by straight lines representing the results of Eq. 22 for Λ.

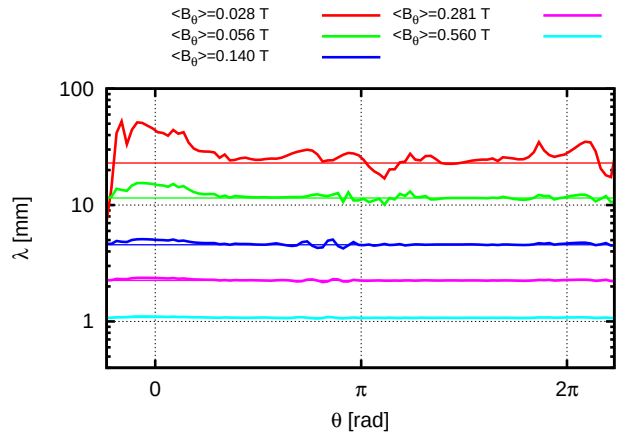

FIG. 9 (Color online) Dependence of Λ on the poloidal magnetic field $\hat{B}_\theta$. Shown are the profiles of the inverse logarithmic derivatives $|\partial \ln n/\partial r|^{-1}$ overlaid by straight lines representing the results of Eq. 22 for Λ.

VI. SOL WIDTH IN PARAMETER SCAN

In this section results from 2D simulations are presented to examine whether the details of the X-point geometry have some effect on the basic relations $\Lambda\sim T^{1/2}$ and $\Lambda\sim\hat{B}_\theta^{-1}$ expressed in Goldston's estimate. Several simulations have been conducted for the ASDEX like geometry with parameters chosen as in Section IV but firstly for varying temperatures 5 eV $\leq T\leq$ 500 eV and secondly for varying poloidal magnetic field, i. .e. varying value of C in a range such that 0.028 T$\leq\langle\hat{B}_\theta\rangle\leq$0.56 T. The results for the profiles of the decay length $|\partial \ln n/\partial r|^{-1}$ are shown in in Figs. 8 and 9 in logarithmic plots. For comparison also the result from Eq. 22 are shown where Λ has been obtained by numerical integration between the central transition points. It can be seen that the decay length obtained by the logarithmic derivative of the numerical profiles of the density in the SOL is

to a large extent constant along the poloidal angle. Also it is obvious that the values of Λ follow closely the expected functional dependence on T and $\hat{B}_\theta$ described by Eq. 22. However, in some cases the precise values of Λ can differ by a factor of 2-4 for inner and outer target and with respect to the analytical result from Eq. 22, especially for low $\langle \hat{B}_\theta \rangle$. In summary it can be concluded that the numerical results confirm the linear functional dependance on the poloidal Larmor radius ρ_p

$$\Lambda \sim \rho_p, \quad \rho_p = \sqrt{\frac{2Tm_i}{e^2 \hat{B}_\theta^2}} \tag{25}$$

but uncertainties remain concerning the proportionality constant and in some cases the assumption of an overall decay length is not justified. However, for most of the cases considered the expression Eq. 22 gives a very precise estimate for the SOL width found in the 2D simulations.

VII. DIFFUSIVE TRANSPORT AND SOL WIDTH

In this section 2D results from simulations including homogeneous diffusive particle feeding of the SOL are presented. For this purpose the model equations Eq. 1 and 11 are modified as follows (particle sources S_n neglected)

$$\frac{\partial n}{\partial t} + \boldsymbol{\nabla} \cdot (n\mathbf{u}_\parallel) + \boldsymbol{\nabla} \cdot (n\mathbf{u}_*) = \boldsymbol{\nabla} \cdot (\mathbf{D}_\perp \cdot \boldsymbol{\nabla} n) \tag{26}$$

$$\begin{aligned} &\frac{\partial n}{\partial t} + \frac{1}{J}\frac{\partial}{\partial \theta}\left(J\frac{B^\theta}{B} n u_\parallel + J n u_\times^\theta\right) + \frac{1}{J}\frac{\partial}{\partial r}\left(J n u_\times^r\right) \\ &\quad = \frac{1}{J}\frac{\partial}{\partial r}\left(J\frac{D_\perp}{g_{rr}}\frac{\partial n}{\partial r}\right) \end{aligned} \tag{27}$$

where $D_\perp$ is a constant diffusion coefficient. The results for varying values of $D_\perp$ in the range between 0.001 m^2/s and 0.5 m^2/s are shown in Fig. 10. Again the profiles of the inverse logarithmic derivative of the density are shown. For low values of $D_\perp$ the profiles are rather flat but for higher values of $D_\perp$ the assumption of a constant Λ is not justified anymore. For further analysis also the averaged values of the numerically obtained decay length are shown a straight horizontal lines in Fig. 10. Despite the detailes of the profiles of the decay lengths it is obvious that additional diffusion increases the SOL width Λ changes significantly for $D_\perp$>0.01 m^2/s. For $D_\perp$=0.2 m^2/s it is about a factor of 5 larger than the drift-based value. It is to be noted that the supersonic transitions do not disappear completely for the range of $D_\perp$ considered. The averaged values $\langle \Lambda \rangle$ (the straight horizontal lines in Fig. 10) are plotted again in Fig. 11 as a function of $D_\perp$. This plot is complemented by a fit based on the functional $\Lambda = \Lambda_0 \left(1 + \sqrt{1 + D_\perp/D_*}\right)/2$. which is motivated by the following extension of the 1D model. Using the

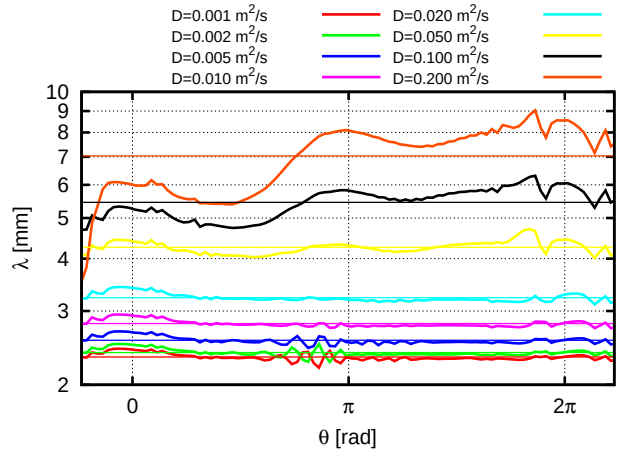

FIG. 10 (Color online) Dependence of Λ on the additional particle diffusion characterized by $D_\perp$. Shown are the profiles of the inverse logarithmic derivatives $|\partial \ln n/\partial r|^{-1}$ overlaid by straight lines representing its respective θ-averaged value.

same assumptions as in Section V the equation Eq. 15 is replaced by

$$u_\parallel \frac{\partial n}{\partial \theta} = -n\frac{\partial u_\parallel}{\partial \theta} + \frac{B}{B^\theta}\left(\frac{u_\times^r}{\Lambda} + \frac{D_\perp}{\Lambda^2 g_{rr}}\right) n \tag{28}$$

and the equation for the Mach number M becomes

$$M - \frac{M^3}{3} = \int \frac{B}{B^\theta}\left(\frac{u_\times^r}{\Lambda c_s} + \frac{D_\perp}{\Lambda^2 g_{rr} c_s}\right) d\theta + C_M \tag{29}$$

Therefore, a quadratic equation for Λ results

$$c_2 \Lambda^2 - c_1 \Lambda - c_0 D_\perp = 0 \tag{30}$$

where

$$c_2 = M_2 - \frac{M_2^3}{3} - M_1 + \frac{M_1^3}{3} \tag{31}$$

and

$$c_1 = \int_{\theta_1}^{\theta_2} \frac{B u_\times^r}{B^\theta c_s} d\theta, \quad c_0 = \int_{\theta_1}^{\theta_2} \frac{B}{B^\theta g_{rr} c_s} d\theta \tag{32}$$

Here M_1=$M(\theta_1)$ and M_2=$M(\theta_2)$ are the Mach numbers at the integration boundaries. The problem in solving equation Eq. 30 is the lack of appropriate integration limits θ_1 and θ_2. In Section V the transition points with $|M|$=1 offered a reasonable choice. For the drift-diffusive problem of Eq. 29 such a choice is not obvious. However, the solution of Eq. 30 can be written in the form

$$\Lambda = \frac{\Lambda_0}{2}\left(1 + \sqrt{1 + \frac{D_\perp}{D_\perp^*}}\right) \tag{33}$$

with Λ_0 the decay length in drift limit and $D_\perp^*$ a scaling diffusion coefficient

$$\Lambda_0 = \frac{c_1}{c_2}, \quad D_\perp^* = \frac{c_1^2}{4 c_0 c_2} \tag{34}$$

This gives reason to the particular fit function used in Fig. 11. which gives Λ_0=2.27 mm and D_*=8.08·10^{-3} m^2/s. Therefore, even a particle diffusion of $D_\perp$=0.01 m^2/s, which is relatively low compared to typical edge transport simulations, is enough to cover the effects of drift-based transport and its related SOL width completely. This is of importance for future studies with more sophisticated numerical approaches. Also the existence of transition points located at $u_\times^r$=0 might give a hint for experimental proof of the dominance of the drift-based particle transport underlying the heuristic model of Goldston.

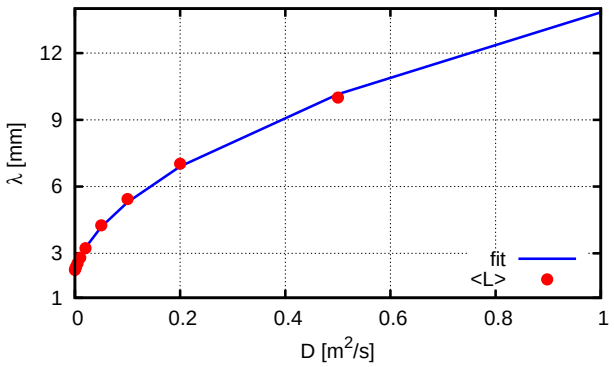

FIG. 11 (Color online) Dependence of Λ on the additional particle diffusion characterized by $D_\perp$. The points in red are the θ-averaged values $\langle|\partial \ln n/\partial r|^{-1}\rangle$ as found in Fig. 10 from the numerical solution of the 2D model. The blue line represents a fit of the form $\Lambda_0/2\left(1+\sqrt{1+D_\perp/D_*}\right)$ motivated by the 1D estimate Eq. 33 with fit parameters Λ_0=2.27 mm and D_*=8.08·10^{-3} m^2/s.

VIII. CONCLUSIONS

- The parametric dependence of Goldston's estimate for the scrape-off particle width has been assessed by 2D simulations in X-point magnetic configurations supported by a 1D approximative model. The functional dependencies of Goldston's λ-formula have been confirmed.
- The simulations indicate that in situations where the radial particle transport in the SOL is dominated by the diamagnetic drift effect supersonic transitions are likely to occur. Even though a supersonic transition can be caused also by magnetic compression effects. On the other hand, the particular location for such a transition to occur is inevitably connected with the points where the radial drift is zero in case the drift-based transport is dominant. This differs completely from the diffusion dominated case and might give a hint for experimental proof.
- The inverse $\hat{B}_\theta$ dependence is confirmed but for a quantitative calculation of the scrape-off width it is of importance to use the local value in the region of particle inflow from the core into the SOL to get the right proportionality factor.
- An additional particle diffusion increases the decay length Λ significantly even for moderate diffusivities compared to typical values used for anomalous diffusion in transport codes. Therefore, studies on the drift-based effects should be pushed to the numerically more challenging limit of very small particle diffusion in the range of $D_\perp$~10^{-2} m^2/s and beyond.

Acknowledgments

This work has been carried out within the framework of the EUROfusion Consortium and has received funding from the Euratom research and training programme 2014-2018 under grant agreement No 633053. The views and opinions expressed herein do not necessarily reflect those of the European Commission.

References

[1] R. J. Goldston, Nucl. Fusion 52, 013009, 2012
[2] T. Eich et al., Nucl. Fusion 53, 093031, 2013
[3] M. Faitsch et al., Plasma Phys. Control. Fusion 57, 075005, 2015
[4] T. D. Rognlien et al., J. Nucl. Mat. 266-269, 654-659, 1999
[5] V. A. Rozhansky et al., Nucl. Fusion 41, 387, 2001
[6] A. Kurganov and E. Tadmor, J. Comp. Phys. 160, 241-282, 2000

APPENDIX A: Magnetic field configuration and conformal mapping

A conformal map $R+iZ=f(r,\theta)$ is defined where R and Z are related to Cartesian coordinates via

$$x = R\cos\phi, \quad y = R\sin\phi, \quad z = Z \tag{A1}$$

and f is chosen as

$$f = \left(R_0 - e^{-i\vartheta}\sqrt{r^2 - h^2\, e^{2i\vartheta}}\right) e^{i\xi} + \left(1 - e^{i\xi}\right)(R_0 + iZ_0) \tag{A2}$$

The coordinate ϑ is given as a function of θ

$$\vartheta = \frac{\pi}{2\,\mathrm{erf}(3\pi/s)}\left[\mathrm{erf}\left(\frac{3\pi}{s}\right) - \mathrm{erf}\left(\frac{3\,\pi-\theta}{s}\right) + \mathrm{erf}\left(\frac{\pi+\theta}{s}\right) - \mathrm{erf}\left(\frac{\pi-\theta}{s}\right)\right] \tag{A3}$$

The Eqs. A1-A3 define the transformation between the coordinate functions (x,y,z), (R,ϕ,Z) and (r,θ,ϕ). Due to the properties of conformal maps the coordinates (r,θ,ϕ) are right-handed orthogonal. Their coordinate

lines are similar to tokamak X-point geometries with X-point being located at $r{=}h$ and $\theta{=}0$. This mapping of an X-point tokamak field onto an orthogonal grid in the (r,θ)-plane is particularly suitable for numerical approaches. Note that for $h{\to}0$, $\partial\vartheta/\partial\theta{=}1$, a circular geometry is recovered. The parameters R_0, Z_0, ξ and s are introduced to translate and rotate the grid and to control the resolution close to the X-point. The point (R_0, Z_0) defines the center of rotation in the (R, Z)-plane and ξ denotes the rotation angle. A parameter $s{>}1$ is used to increase the density of grid points close to the X-point while the grid points are still equidistant on the θ-coordinate lines. An example of a resulting grid is shown in Fig. 1. The tranformation is characterized by the Jacobian $J{=}\mathbf{e}_r \cdot \mathbf{e}_\theta \times \mathbf{e}_\phi$

$$J = \frac{R}{r}\frac{\partial\vartheta}{\partial\theta}\frac{r^4}{\sqrt{r^4 - 2\,h^2\,r^2\,\cos 2\vartheta + h^4}} \tag{A4}$$

and the metric coefficients g_{rr}, $g_{\theta\theta}$ and $g_{\phi\phi}$

$$g_{rr} = \frac{J}{rR}\frac{1}{\partial\vartheta/\partial\theta}, \quad g_{\theta\theta} = \frac{rJ}{R}\frac{\partial\vartheta}{\partial\theta}, \quad g_{\phi\phi} = R^2 \tag{A5}$$